Redox transformations of Ru catalyst during NO oxidation at industrial nitric acid production conditions

Jithin Gopakumar [a], Pål Martin Benum [a], Ingeborg-Helene Svenum [b], Bjørn Christian Enger [c], David Waller [d], Magnus Rønning [a,*]

[a] *Norwegian University of Science and Technology (NTNU), Department of Chemical Engineering, Sem Sælands vei 4, NO-7491 Trondheim, Norway*
[b] *SINTEF Industry, Materials and Nanotechnology group, P.O. Box 4760 Torgarden, NO-7465 Trondheim, Norway*
[c] *SINTEF Industry, Kinetic, and Catalysis group, P.O. Box 4760 Torgarden, NO-7465 Trondheim, Norway*
[d] *YARA Technology Center, Herøya Forskningspark, Bygg 92, Hydrovegen 67, NO-3936 Porsgrunn, Norway*
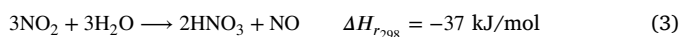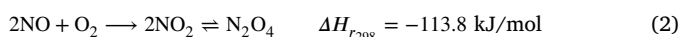
ARTICLE INFO

ABSTRACT

Oxidation of nitric oxide is one of the main steps in the Ostwald process for industrial nitric acid production. This work summarises the use of γ-Al$_2$O$_3$ supported Ru catalyst to study the oxidation of NO to NO$_2$ at ambient and 4 bar pressure with a feed of 10% NO, 6% O$_2$, 15% H$_2$O, and rest Ar. The catalyst was synthesised using wet impregnation and characterised by BET, CO chemisorption, H$_2$-TPR, XPS, XRD, *in-situ* XAS-XRD and DRIFTS. We report the activity and kinetics of supported ruthenium catalyst for NO oxidation under realistic nitric acid plant conditions. The catalyst exhibited a promising low-temperature activity of 72% at 340 °C in complete nitric acid condition and 37% at 420 °C in partial nitric acid condition. An apparent activation energy of 152 kJ/mol was observed and the overall rate was determined to be $r = \frac{k_f \cdot K_G \cdot P_{NO}^2 \cdot P_{O_2}}{P_{NO_2}}$, where k_f and K_G represents forward rate and equilibrium rate constants respectively. The reaction was found to be second order with respect to NO, first order with respect to O$_2$ and inversely dependent on NO$_2$ partial pressure. The stability of the catalyst was also tested during 45 h of isothermal NO oxidation at ambient pressure. From *in-situ* XAS-XRD and DRIFTS experiments it was revealed that during isothermal NO oxidation the reaction oscillates as the ruthenium surface goes through redox cycles. A plausible reaction mechanism that fits with our experimental observations and the oxidative nature of ruthenium is proposed. This study demonstrates and explains the capacity of supported ruthenium catalysts to oxidise NO to NO$_2$ in industrial nitric acid production conditions.

1. Introduction

Nitric acid is a corrosive mineral acid, mainly used to produce nitrate fertilisers, an essential that dramatically improves the agricultural output in modern agrarian systems [1,2]. Commercial nitric acid production uses the Ostwald process, which consists of three important chemical steps, (a) catalytic oxidation of ammonia using Pt-Rh gauze (Eq. (1)), followed by gas-phase oxidation of NO to NO$_2$ using series of heat exchangers (Eq. (2)), and finally NO$_2$ absorption in water to produce nitric acid (Eq. (3)) [3–5].

$$4NH_3 + 5O_2 \longrightarrow 4NO + 6H_2O \qquad \Delta H_{r_{298}} = -907 \text{ kJ/mol} \qquad (1)$$

$$2NO + O_2 \longrightarrow 2NO_2 \rightleftharpoons N_2O_4 \qquad \Delta H_{r_{298}} = -113.8 \text{ kJ/mol} \qquad (2)$$

$$3NO_2 + 3H_2O \longrightarrow 2HNO_3 + NO \qquad \Delta H_{r_{298}} = -37 \text{ kJ/mol} \qquad (3)$$

Modern nitric acid plants are either mono (7–12 bar) or dual-pressure (4–5 bar for ammonia oxidation, NO$_2$ absorption usually at higher pressure, 10–15 bar). The gas composition after ammonia oxidation (Eq. (1)) contains 10% of NO, along with 6% O$_2$ and 15% H$_2$O [3–5]. With such oxidising and corrosive conditions, the development of stable catalysts is challenging. The gas-phase NO to NO$_2$ oxidation reaction (Eq. (2)) has an inverse dependence on temperature and thus, low temperatures favour NO$_2$ formation [3] and the product NO$_2$ starts to decompose to NO and O$_2$ at temperatures above 275 °C [6]. Hence, designing an industrially relevant catalyst for NO oxidation at these conditions will require a catalyst that can attain equilibrium conversion at lower temperatures for higher energy recovery [7]. Industrial use of catalysts for oxidising NO to NO$_2$ has several advantages, (1) it decreases capital expenditure (CAPEX), (2) thus reducing industrial footprint, and (3) enables significant-high-quality heat recovery [7].

Apart from the earlier publications by our group at dry nitric acid conditions [8,9], wet nitric acid conditions [10] and Grande et al. [7], only a few other early patents discuss catalytic oxidation of NO to NO_2 at conditions relevant to nitric acid production [11–13].

A large body of existing research on nitrogen oxides is focused on catalytically oxidising and reducing NO at diesel exhaust or low NO concentration conditions, typically 0.01%–1% of NO and 0.1%–20% of O_2. Various catalysts, ranging from metal oxides, noble metals, and perovskites have been investigated at these conditions [14]. Pt is one of the noble metals that has been extensively studied for NO oxidation. Salman et al. [8] also studied NO to NO_2 oxidation at ambient pressure in the absence of water and reported zero-order on NO partial pressure and half-order dependency on oxygen. A Langmuir-Hinshelwood model was proposed with the NO_2 desorption step as the rate-limiting step. However, Mulla et al. and Weiss et al. [15,16] reported reaction orders of 1,1 and −1 for NO, O_2 and NO_2 respectively. Olsson et al. studied both Langmuir-Hinshelwood, Eley-Rideal and a combination of both models on NO oxidation and reported that there is not one true model for NO oxidation on alumina-supported platinum catalysts [17,18]. Under strong oxidising conditions, platinum tends to lose its activity due to the formation of platinum oxide [19]. A typical feed composition after industrial ammonia oxidation is 10% NO, 6% O_2, 15% H_2O and rest N_2, which is strongly oxidising conditions. As a result, platinum catalysts are not so reliable for NO oxidation at these concentrations. In addition, the high cost and limited availability of platinum make it a bottleneck for becoming an industrial catalyst for NO oxidation at nitric acid conditions.

Supported ruthenium catalysts have been widely used and researched for ammonia synthesis, and NO to NO_2 oxidation at low concentrations of NO and various other oxidation reactions [20–23]. However, to the best of our knowledge there is no research published on supported Ru catalysts for NO oxidation at industrial nitric acid production conditions. This paper reports the NO oxidation activity of γ-Al_2O_3-supported Ru catalysts at conditions relevant to industrial nitric acid production. Supported Ru catalysts presented promising activity at ambient and 4 bar pressures. In addition, activation energy along with reaction orders with respect to NO, NO_2, O_2, and H_2O were investigated at ambient pressure, and a suitable reaction mechanism is proposed.

2. Experimental

2.1. Catalyst preparation

The ruthenium catalyst was prepared using wet impregnation. Commercial γ-Al_2O_3 (Alfa Aesar GmBH) pellets were crushed and sieved to 53–90 μm sieve fraction. To prepare 0.5 wt.% Ru catalyst, the γ-Al_2O_3 support was impregnated in one-step by calculated amounts of $RuCl_3 \cdot xH_2O$ (Sigma-Aldrich) in de-ionised water. The catalyst was dried in ambient air at 120 °C for 12 h and calcined in a flow of synthetic air (50 N cm^3/min) at 400 °C (heating rate of 5 °C/min) for 2 h and subsequently cooled inside the calcination reactor. The calcined catalyst was again crushed and sieved to 53–90 μm sieve fraction. The catalysts are designated as Ru_x, where x corresponds to the conditions that the catalyst samples are subjected to and are defined in Table 1. Fig. 1 depicts different programs and conditions the catalysts are subjected to and how the catalyst samples are designated. Fig. 8(a) presents program and catalyst sample designation for *in-situ* XAS-XRD experiments.

2.2. Catalyst characterisation

Elemental analysis of the as-prepared catalyst was determined by inductively coupled plasma optical emission spectroscopy (Agilent 8900 Triple Quadrupole ICP-MS (ICP-QQQ) with SPS 4 Autosampler). Prior to ICP analysis, HCl (6 ml)/HNO_3(0.1 ml) was used to mineralise the

Table 1
Ruthenium catalyst samples (Ru_x) designation.

x	Definition
F	Fresh sample
C	Calcined sample in air at 400 °C for 2 h
SP	Spent sample
LT	Longer isothermal run in a feed of 10% NO, 6% O_2, 15% H_2O and rest Ar at 350 °C for 45 h
ST	Short isothermal run in a feed of 10% NO, 6% O_2, 15% H_2O and rest Ar at 350 °C for 3 h
Red	Reduced sample in a feed of 5%H_2/Ar at 400 °C in a temperature ramp of 50–400 °C
NO	Subjected to a temperature ramp of 150–450 °C in a feed of 10% NO, 6% O_2, 15% H_2O and rest Ar

samples for 60 min at 250 °C in a Milestone UltraWAVE microwave digestor.

N_2 adsorption was used to measure the specific surface area of the catalyst samples. 100 mg of each sample were degassed at 200 °C overnight in a VacPrep 061 Degasser before transferring to a Micromeritics TriStar II 3020 Surface Area and Porosity Analyser. Specific surface areas and pore volumes were calculated using BET and BJH (desorption) methods at liquid nitrogen temperature (−196 °C).

Ex-situ X-ray diffractograms for the catalyst samples and the support were obtained using a Bruker D8 Advance X-ray Diffractometer (D8 Davinci) at 40 kV and 40 mA, using the wavelength of Cu K_α radiation (1.54060 Å). The diffractograms were recorded in the 2θ range of 5–75° with a 0.1° slit opening.

H_2-temperature programmed reduction (TPR) was performed using an Altamira Bench- CAT Hybrid 1000 HP in a U-shaped quartz reactor in order to verify and tune the catalyst reduction/pre-treatment procedure. Before TPR, 100 mg of the catalyst was pre-treated with a flow of argon (40 N cm^3/min) at 150 °C for 30 min with a heating rate of 10 °C/min. The reduction was performed as a temperature scan from 50 to 400 °C with a heating rate of 5 °C/min with a flow of 40 N cm^3/min of 5%H_2 in Ar.

CO chemisorption measurements were recorded using a Micromeritics ASAP 2010S unit at 30 °C for fresh and spent samples of the catalyst [24]. $Ru_{F,C,Red}$ catalyst sample of known weight was loaded into a U-shaped quartz reactor and the bed temperature was controlled using a thermocouple. Before chemisorption, the sample was dried at 100 °C for 30 min. The isotherm was measured in the pressure range of 150–400 mmHg. The Ru dispersion was calculated based on strongly adsorbed CO, assuming an adsorption ratio of 1 for CO/Ru [24,25].

X-ray photoelectron spectroscopy (XPS) was used to study the ruthenium surface species present on the catalyst. A few milligrams of the catalyst samples were mounted on a carbon tape and an Axis Ultra^{DLD} XP spectrometer (Monochromatic Al Kα radiation with $h\nu$ = 1486.6 eV) from Kratos Analytical was used for the analysis, with a sample analysis area about 700 × 300 μm. The pass energy and step length used for measuring the survey spectrum are 160 eV and 1 eV, respectively. For measuring individual core levels, a pass energy of 40 eV was used and a step length of 0.1 eV. Charge compensation was applied during spectra acquisition and the binding energy scale was calibrated to the Al 2p component of the γ-Al_2O_3 support at 74.5 eV. The data treatment for all collected data was performed using CasaXPS [26]. The line profiles for oxidised and metallic ruthenium as found by Morgan [27] were used in the fitting of the ruthenium components. Fig. S24 presents the survey spectrum of all analysed catalyst samples and the γ-Al_2O_3 support. A trace amount of Cl was detected for most of the samples including the γ-Al_2O_3 support.

In-situ X-ray absorption spectroscopy (XAS) experiments at the ruthenium K edge (22.1172 keV) were carried out at the Swiss-Norwegian Beamlines (SNBL) BM31 at the European Synchrotron Radiation Facility (ESRF), France. The experimental setup is presented in Fig. S4. A quartz capillary of 0.1 cm internal diameter was loaded with
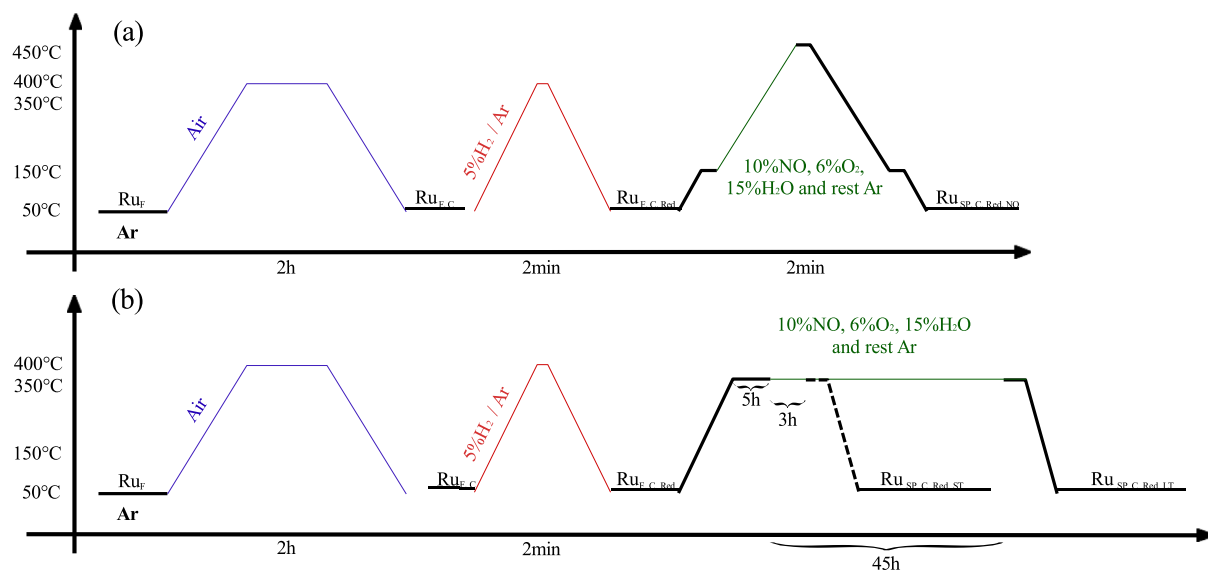
Fig. 1. Designations of 0.5 wt.% Ru on γ-Al$_2$O$_3$ support (a) during NO oxidation as a function of temperature and (b) during short and long isothermal NO oxidation.

5 mg of Ru$_{F,C}$ catalyst sample with quartz wool on either end of the catalyst bed (bed length = 1 cm). The reactor was then mounted in a custom bracket and exposed to X-rays, with the capillary temperature controlled using a hot air blower. A dedicated setup with mass flow controllers was used to feed desired concentrations of NO, O$_2$, and He (WHSV: 24,000 N cm^3/g$_{cat}$ h; 0.5%NO, 1.3%O$_2$, 0.75%H$_2$O and He balance). To feed water, a sparger system was used assuming complete saturation of oxygen and helium gas mixture. To avoid gas-phase conversion before the bed, a tube in tube of 1/64″ was used to feed NO, such that oxygen, water and helium meet NO at the inlet of the catalyst bed.

In-situ X-ray diffractograms (XRD) were collected with a Pilatus detector (Dectris) using monochromatic radiation ($\lambda = 0.25$ Å). The instrumental peak broadening, wavelength calibration, and detector distance corrections were performed using a NIST 660a LaB$_6$ standard. In the *In-situ* XAS-XRD programme is described in Fig. 8. The catalyst sample was first reduced in a temperature ramp from 50–400 °C (ramp rate of 5 °C/min) in 5% H$_2$/He with 2 min dwell at 400 °C, before being subjected to isothermal NO oxidation with 0.5%NO, 1.3%O$_2$, 0.75%H$_2$O and He balances at 350 °C. X-ray absorption near edge structure (XANES) profiles were recorded during the reduction temperature ramp and isothermal run at 350 °C. Extended X-ray absorption fine structure (EXAFS) was measured before and after the reduction ramp and isothermal run in 100% He flows at 50 °C to analyse the local environment of ruthenium for fresh, reduced and spent catalyst. A lower concentration of NO was used for the *in-situ* studies due to the safety constraints at ESRF. Furthermore, compromises were made due to limitations in the flow ranges of mass flow controllers and the reaction space velocity. For identification and visual comparison purposes of different ruthenium compounds, the Materials Project database was used and is presented in Fig. S13 [28–31], verifies the absence of RuO$_4$ during NO oxidation. Also, the edge step of Ru$_{F,C,Red}$ and Ru$_{SP,C,Red}$ catalyst samples were the same, which confirms that RuO$_4$ was not formed. For EXAFS fitting in Artemis, two ruthenium standards were measured. The EXAFS of ruthenium foil (Ru^0) and RuO$_2$ (Ru^{4+}) (Sigma-Aldrich) powder were measured *ex-situ* in transmission mode. *Ex-situ* X-ray diffractograms of γ-Al$_2$O$_3$ at 50 °C was also recorded for comparison of diffractograms.

In-situ diffuse reflectance infrared Fourier transform spectroscopy (DRIFTS) was used to analyse the surface changes on the Ru$_{F,C,Red}$ catalyst during NO oxidation. The spectra were collected using a Tensor II spectrometer (Bruker Optics), equipped with a liquid N$_2$ cooled mercury cadmium telluride (MCT) detector and a Praying Mantis diffuse

reflectance accessory (Harrick). The reaction was performed inside the Praying Mantis high-temperature reaction chamber with a special flat dome with a KBr window. The inherent dead volume of the reaction chamber was reduced by filling the voids with SiC (1190 μm) and thus reducing the gas-phase conversion to 10% at 350 °C. Due to the cold spots inside the reaction chamber, NO oxidation was conducted in the absence of water vapour. 50 mg of the Ru$_{F,C,Red}$ sample was loaded into the reaction chamber. The spectra were measured between 4000–600 cm^{-1} with a spectral resolution of 4 cm^{-1}. Prior to the reaction, the background/reference spectra were collected with 32 scans on the Ru$_{F,C,Red}$ catalyst at 350 °C in 100% Ar (WHSV: 24,000 N cm^3/g$_{cat}$ h). A step-response experiment (as presented in Fig. S18) with a 6 min duration for each step was performed on the Ru$_{F,C,Red}$ catalyst to identify the types of surface evolving species in the presence of NO or O$_2$ in Ar at 350 °C. Isothermal NO oxidation was also performed at 350 °C in 10% NO, 6% O$_2$ and balance Ar (WHSV: 24,000 N cm^3/g$_{cat}$ h) for 30 min. Prior to the isothermal NO oxidation, the catalyst samples were dwelled at 350 °C in 100% Ar for 30 min and respective DRIFT spectra were collected. After isothermal NO oxidation, DRIFT spectra were collected at 350 °C in 100% Ar for 30 min. The outlet gas composition of NO, N$_2$O and NO$_2$ was monitored using an infrared gas analyser (MKS MultiGas 2030-HS FTIR Gas Analyser, 5.11 m path length).

The Multivariate Curve Resolution-Alternating Least Square (MCR-ALS) package in Python (3.10) was used for analysing the collected DRIFTS data and XANES data for the catalyst during the isothermal run to obtain distinct components in the data [32]. A Savitzky-Golay filter from SciPy was used for representing an extract of contribution plots obtained from MCR-ALS for XANES data [33]. Athena and Artemis, part of the Demeter software package, were used to analyse all MCR-ALS extracted XANES components and EXAFS [34]. EXAFS data of Ru$_{F,C,Red}$ and Ru$_{SP,C,Red}$ were processed in Athena first, with the input parameter for background subtraction R$_{bkg}$ to be 1.1–1.3 Å. Artemis was used to fit Ru^0, RuO$_2$, Ru$_{F,C,Red}$ and Ru$_{SP,C,Red}$ Ru-Ru and Ru-O paths in k-space using k$_w$ = 3 and fitting window of 3–15.1 k, to find respective coordination numbers for shells in the R range of 1.0–4.0 Å.

2.3. Experimental set-up for catalytic activity measurement

The experimental set-up and reactor details are given in our previous publications [8,9]. To summarise, an illustration of the experimental setup is presented in Fig. S1. All reactant gases for catalytic testing (NO, O$_2$, NO$_2$, H$_2$ and Ar) were obtained from Linde-Gass AS. Water

vapour was controlled and fed using a controlled evaporator mixer (CEM) from Bronkhorst. All gas lines before and after the reactor are preheated to 200 °C, to ensure no cold spots for water condensation. A back pressure regulator was introduced downstream of the reactor to conduct experiments at 4 bar. A stainless-steel tubular reactor of 9.7 mm inner diameter was used for activity testing. The catalyst bed was loaded with 0.5 g of catalyst and 2.75 g of SiC sandwiched between wads of quartz wool. SiC was chosen to be a diluent as it is inactive during NO-oxidation [8]. For heating the reactor, a heat block is used with four cartridge heaters controlled by a Eurotherm. Two thermocouples, T_1 and T_2 are placed in the catalyst bed and heat block, respectively for precise control of the temperature. For catalytic activity testing with respect to temperature, the catalyst bed temperature (thermocouple — T_1) was controlled using a Eurotherm controller. A high precision back pressure regulator (ULHT Equilibar BPR) was used for carrying out 4 bar pressure experiments. Pretreatment includes reducing the catalyst bed at 400 °C with 5%H_2/Ar flowing at a space velocity of 24,000 N cm^3/g$_{gcat}$ h and subsequently cooling down to 150 °C inside the reactor.

Catalyst performance was evaluated as a function of temperature (150–450 °C) and NO to NO_2 conversion in 10% NO, 6% O_2, 15% H_2O and rest Ar feed conditions with a space velocity of 24,000 N cm^3/g$_{gcat}$ h. Tests were performed with the same feed composition at ambient and 4 bar pressure. Due to the limitations of the BPR diaphragm, for catalytic testing at 4 bar pressure the maximum bed temperature was restricted to 400 °C. An infrared gas analyser (MKS MultiGas 2030-HS FTIR Gas Analyser, 5.11 m path length) is used to analyse the product stream and a mass spectrometer (Pfeiffer Vacuum ThermoStar GSD 301 T3 Benchtop Mass Spectrometer) is used to monitor Ar and homonuclear diatomic molecules such as O_2 and N_2. The measurements of thermocouples (T_1 and T_2), FTIR and mass spectrometer are all in real-time with a precision of milliseconds. Additionally, the time gap between the FTIR and mass spectrometer is corrected by pulsing 5%NO_2 in inert.

Conversion of NO to NO_2 (%) is calculated as:

$$NO_{Conversion} = x_{NO} = \lambda \cdot \frac{[NO]_{inlet} - [NO]_{outlet}}{[NO]_{inlet}} \cdot 100 \qquad (4)$$

$$NO_{Catalytic\ Conversion} = NO_{Conversion} - NO_{Gas\text{-}Phase\ Conversion} \qquad (5)$$

where $[NO]_{inlet}$ and $[NO]_{outlet}$ are the inlet and outlet concentration of NO of the reactor. $\lambda = 0.99$, accounts for the volume changes that arise from the reaction [35]. Calculations of reaction orders and apparent activation energy were performed at ambient pressure and catalytic NO to NO_2 conversion was restricted below 15%. The apparent activation energy was calculated with a feed composition of 10% NO, 6% O_2, 15% H_2O and rest Ar, at WHSV = 24,000 N cm^3/g$_{gcat}$ h at 1 bar in the temperature range of 340–366 °C with a catalytic conversion below 12% using Arrhenius plot. Prior to each reaction order measurement, the catalyst bed temperature was stabilised at 350 °C for 2 h in a feed of 100% Ar and reduced in 5%H_2/Ar for 2 h to ensure that the catalyst was in oxidation state Ru^0. The approach to equilibrium (β) was calculated as $(P_{NO_2}/(P_{NO}xP_{O_2}^{0.5}xK_{eq(T)})$, where $K_{eq(T)}$ is the equilibrium constant [15]. The values of β were in the range (0.0003–0.14), which verifies that the applied reaction conditions are far from equilibrium at 350 °C and ambient pressure.

Longer isothermal runs were performed with 10% NO, 6% O_2, 15% H_2O and rest Ar, at WHSV = 24,000 N cm^3/g$_{gcat}$ h for 45 h at 350 °C. To understand the temperature changes in the bed, the heat block temperature (thermocouple - T_2) was controlled and constant power required for the catalyst bed to be at 350 °C was provided. Prior to the long-term tests, heat block temperatures were raised from ambient to 350 °C and dwell-ed up until the temperature in the catalyst bed stabilised at 350 °C in 100% Ar flow. To ensure uniform heating from the heat block to the catalyst bed, a 5-h isothermal run in inert flow at WHSV = 24,000 N cm^3/g$_{gcat}$ h was maintained. The temperature control profile for the catalyst bed in an inert atmosphere is presented in Fig. S2 and the respective confidence interval fit during isothermal operation (controlling thermocouple - T_2) is presented in Fig. S3.

3. Results and discussion

3.1. Chemical and structural characterisation

Table 2 catalogues physisorption, dispersion and elemental analysis results of the catalyst samples and commercial gamma-alumina support respectively. Impregnation of γ-Al_2O_3 with 0.5 wt.% Ru decreased the total surface area to 230 m^2/g. The surface area of Ru$_{F,C,Red}$ catalyst remained similar to the Ru$_{F,C}$ catalyst sample, illustrating no loss in the total surface area while reducing the catalyst. Spent Ru$_{F,C}$ after activity testing at 4 bar pressure had similar dispersion to that of Ru$_{SP,C,Red,NO}$ and Ru$_{F,C,Red}$ catalyst samples, indicating no significant deactivation due to sintering.

Fig. 2 presents X-ray diffractograms of the γ-Al_2O_3 support, with Ru$_{F,C}$, Ru$_{F,C,Red}$, Ru$_{SP,C,Red,NO}$ and Ru$_{SP,C,Red,LT}$ catalyst samples recorded in Cu K$_\alpha$ radiation (1.54060 Å). The diffractogram of the Ru$_{SP,C,Red,NO}$ catalyst sample was collected after activity testing at ambient pressure (see Fig. 5). There were no notable differences in the X-ray diffractograms of the spent samples at ambient and 4 bar pressure tests. For comparing and analysing diffractograms, the ICDD PDF-XRD database was used. From the measured diffractograms, the γ-Al_2O_3 support appears to be less crystalline, and clear RuO$_2$ peaks (marked as * in Fig. 2) can be seen in the Ru$_{F,C}$ catalyst sample when compared to the XRD-PDF database. The appearance of highly crystalline RuO$_2$ diffraction peaks in the diffractogram of the Ru$_{F,C}$ catalyst indicates the formation of bulk RuO$_2$. No diffraction peaks corresponding to metallic Ru were found for Ru$_{F,C}$. However, Ru$_{F,C,Red}$, Ru$_{SP,C,Red,NO}$ and Ru$_{SP,C,Red,LT}$ samples had only diffraction peaks corresponding to metallic Ru (marked as ♦ in Fig. 2) and not RuO$_2$. The Ru$_{SP,C,Red,NO}$ catalyst sample had additional peaks at 36, 38 and 72° corresponding to SiC (marked as ■ in Fig. 2) from the experiment. The intensity of Ru^0 peaks was weaker in Ru$_{SP,C,Red,NO}$, Ru$_{SP,C,Red,LT}$ compared to Ru$_{F,C,Red}$ and the absence of RuO$_2$ peaks suggests surface oxidation or presence of amorphous RuO$_2$. The isothermal NO oxidation experiment was repeated with another sample of Ru$_{F,C,Red}$ catalyst for 2 h without SiC dilution, which resulted in the same degree of Ru^0 diffraction peak intensity reduction, which indicates that the reduction in diffraction peak intensity is not due to dilution.

H_2-TPR was performed on the Ru$_{F,C}$ catalyst sample to understand the reducibility of the catalyst and to confirm the reduction treatment. From literature, Narkhede et al. and Balint et al. observed a three-step reduction profile for unsupported Ru-based nanoparticles with a complete reduction of RuO$_2$ to Ru at 284 °C [36,37]. However, the H_2-TPR profile of the Ru$_{F,C}$ catalyst shows a two-step reduction (see Fig. 3) where the low-temperature peak is associated with the removal of surface oxygen and the high-temperature peak is associated with bulk RuO$_2$ reduction [38,39]. A complete reduction of the Ru$_{F,C}$ catalyst is observed at 250 °C, similar to earlier observations [22,40]. From the XRD diffractograms of Ru$_{F,C}$ and Ru$_{F,C,Red}$ (presented in Fig. 2) and the Ru$_{F,C}$ hydrogen TPR profile (presented in Fig. 3), it is evident that RuO$_2$ is reduced to Ru and that the catalyst activation procedure is sufficient to obtain the required metallic phase of ruthenium. H_2-TPR curve of Ru$_{SP,C,Red,NO}$ presents a single peak of reduction which coincides with Ru$_{F,C}$ peak at 98 °C, which can be associated with the presence of surface oxygen. Comparison of the Ru$_{SP,C,Red,NO}$ X-ray diffractogram (see Fig. 2) and the H_2-TPR curve (see Fig. 3), the reduction in Ru peak intensity can be associated with surface oxidation of Ru to form a surface layer of RuO$_2$.

XPS analysis were performed on four catalyst samples, Ru$_{F,C}$, Ru$_{F,C,Red}$, two samples of Ru$_{SP,C,Red,ST}$ and Ru$_{SP,C,Red,LT}$ sample. Two individual 3 h isothermal NO oxidation at ambient pressure were conducted with Ru$_{F,C,Red}$ catalyst sample, where the experiment was terminated when the oscillating catalyst bed temperature was highest and lowest as presented in Fig. 7(d) the spent samples are referred to as Ru$_{SP,C,Red,ST}$ —high or low. Fig. 4 presents C 1s and Ru 3d XPS spectra of Ru$_{F,C}$, Ru$_{F,C,Red}$, two samples of Ru$_{SP,C,Red,ST}$ (high and

Table 2

N_2 physisorption results giving the BET surface area, Ru dispersion from CO chemisorption measurements, and metal loading for fresh Ru catalyst.

Catalyst	Surface area[a] [m^2/g]	Dispersion [%]	CO uptake[a] [μmol g^{-1}]	Ru content[b] [wt.%]
γ-Al_2O_3	255	–	–	–
$Ru_{F,C}$	230	–	–	–
$Ru_{F,C,Red}$	231	17%	16.02	0.42 ± 0.02
$Ru_{SP,C,Red,NO}$	225	20%	18.34	0.39 ± 0.04

[a] Average of two parallel experiments with the same material.

[b] The Ru content was measured by Agilent 8900 Triple Quadrupole ICP-MS (ICP-QQQ).
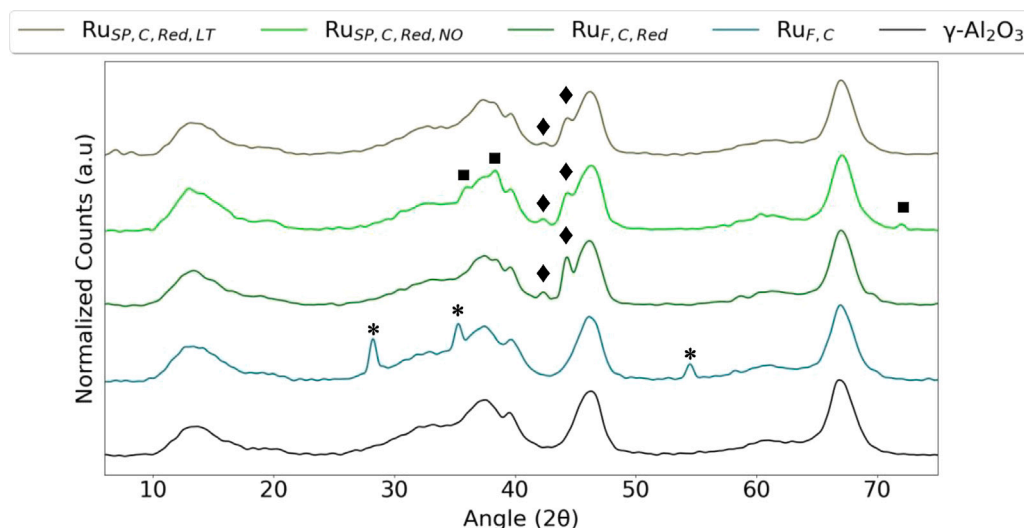
Fig. 2. XRD patterns recorded for the γ-Al_2O_3 support (PDF-00-056-0458), with $Ru_{F,C}$, $Ru_{F,C,Red}$, $Ru_{SP,C,Red,NO}$ and $Ru_{SP,C,Red,LT}$ catalyst samples in the 2θ range 5–75° with Cu K$_\alpha$ radiation (1.54060 Å). Diffraction peaks of SiC (PDF-00-049-1428) are represented as ■, RuO_2 (PDF-04-003-2008) are represented as ∗ and Ru^0 (PDF-00-006-0663) are represented as ◆ respectively.
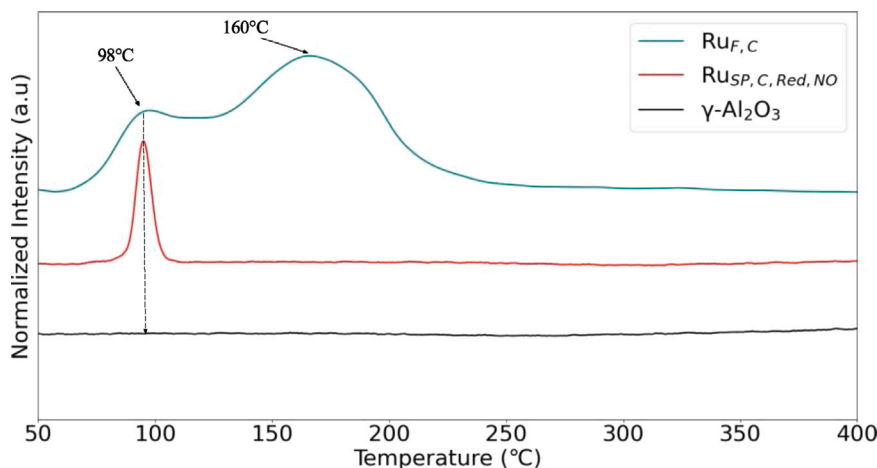

Fig. 3. Stacked normalised H_2-TPR profiles measured for the $Ru_{F,C}$, $Ru_{SP,C,Red,NO}$ catalysts and γ-Al_2O_3 support with 5%H_2/Ar in the temperature range 50–400 °C heated at a rate of 5 °C/min at WHSV = 24,000 N cm^3/g_{gcat} h at ambient pressure.

low) and $Ru_{SP,C,Red,LT}$. Two different contributions associated with metallic ruthenium and oxidised ruthenium can be fitted in the XPS spectra of the catalysts shown in Fig. 4. The Ru $3d_{5/2}$ component of metallic ruthenium is at a binding energy of 279.8 eV, in agreement with Morgan [27]. The main Ru $3d_{5/2}$ component of ruthenium oxide is at 280.4 eV for the $Ru_{F,C}$ catalyst sample (presented in Fig. 4(a)). The fresh $Ru_{F,C}$ catalyst sample had only Ru oxide contribution, however, metallic Ru was found to be the major component for $Ru_{F,C,Red}$, $Ru_{SP,C,Red,LT}$ and the two samples of $Ru_{SP,C,Red,ST}$(high and low). Out of the two high and low-temperature $Ru_{SP,C,Red,ST}$ samples, the only difference in the Ru(3d) spectra was a shoulder peak for $Ru_{SP,C,Red,ST}$

high sample, indicating surface oxidation. The Ru(3d) spectrum of $Ru_{SP,C,Red,ST}$ low is similar to $Ru_{F,C,Red}$ where no trace of Ru oxidation was observed. However, although metallic Ru was the major component for $Ru_{SP,C,Red,LT}$, to achieve a satisfactory fit, a minor contribution of Ru oxide was included.

3.2. Catalytic activity

HSC software [41] was used to simulate equilibrium composition changes with respect to temperature at ambient and 4 bar pressure with 10% NO, 6% O_2, 15% H_2O and balance Ar (presented in Fig.
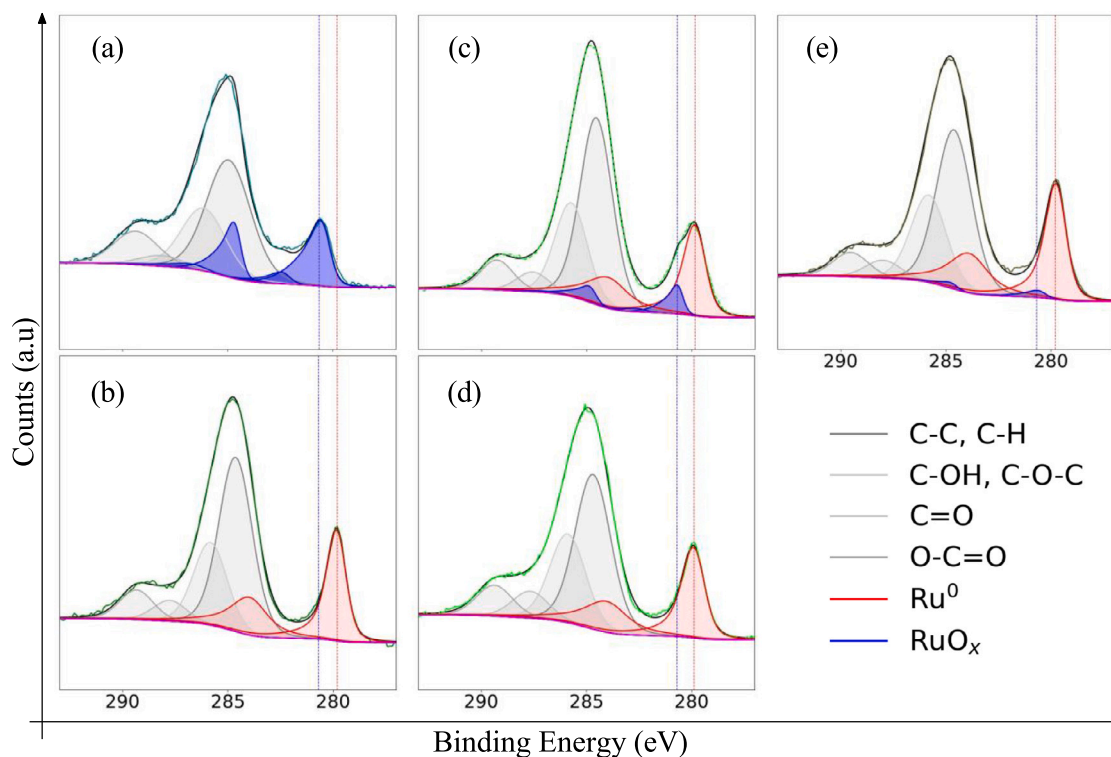
Fig. 4. C 1s and Ru 3d XPS spectra of (a) $Ru_{F,C}$ –, (b) $Ru_{F,C,Red}$ –, (c) $Ru_{SP,C,Red,ST}$ — high - -, (d) $Ru_{SP,C,Red,ST}$ — low – and (e) $Ru_{SP,C,Red,LT}$ – catalyst samples with respective envelope –, background –, carbon and ruthenium peak fits.

S5). The results present RuO_2 to be the most favourable phase along with the presence of nitrous acid and nitric acid. Fig. S8 presents the conversion for $Ru_{F,C,Red}$ and $Ru_{F,C}$ catalyst samples, where $Ru_{F,C,Red}$ dominates $Ru_{F,C}$ conversion indicating metallic Ru to play a vital role in catalyst activity towards NO oxidation. Figs. 5 and 6 show conversion of NO to NO_2 as a function of temperature with 10% NO, 6% O_2, 15% H_2O over the $Ru_{F,C,Red}$ catalyst along with the simulated equilibrium curve (using HSC Chemistry software [41]) and gas phase conversion at ambient and 4 bar pressure, respectively. Prior to activity testing, an empty reactor run was performed (presented in Fig. S6), showing that the NO conversion decreased with increasing temperatures which confirms the inertness of the reactor material and surfaces verifying the inverse Arrhenius behaviour [3]. To record gas phase conversion, the reactor was loaded with only SiC and NO conversion was measured. Activity tests were also conducted using a mix of γ-Al_2O_3 support and SiC and resulted in similar activity as that of the gas phase conversion, which confirmed the inertness of SiC and the support towards NO oxidation in the measured temperature range (presented in Fig. S6). The catalytic activity of the $Ru_{F,C,Red}$ catalyst had an onset temperature of 320 °C at ambient pressure and 220 °C at 4 bar pressure. The maximum conversion is obtained at 420 °C at ambient pressure and at 340 °C in the 4 bar pressure test, after which the reaction becomes thermodynamically limited and follows the equilibrium curve. From comparing NO conversion (%) of a 1 wt.% Pt catalyst on the same support, the 0.5 wt.% Ru catalyst meets the equilibrium conversion at a lower temperature (see Fig. S7), thus exhibiting higher catalytic activity. Bezkrovnyi et al. [42] proposed loss in Ru as volatile RuO_4 during propane oxidation. Before and after the reaction, the fresh and spent catalyst samples along with SiC were weighed to ensure no changes in catalyst mass during catalytic activity. Additionally, ICP analysis was performed on fresh and spent catalyst samples to confirm no significant change in ruthenium loading (see Table 2). *In-situ* XAS results presented in Figs. 9 and 8 in comparison to RuO_4 XAS profile in Fig. S13 verifies absence of RuO_4 during NO oxidation. Also, the edge step of $Ru_{F,C,Red}$ and $Ru_{SP,C,Red}$ catalyst samples were the same, which refutes any theory suggesting the formation of RuO_4.

Table 3
Reaction orders with respect to NO, O_2, NO_2, H_2O partial pressures on the NO oxidation rate at 350 °C with WHSV = 24,000 N cm^3/g$_{gcat}$ h at ambient pressure.

Specie	Reaction order[a]
NO	1.8 ± 0.024
O_2	1.1 ± 0.025
NO_2	-1.0 ± 0.028
H_2O	-0.1 ± 0.016

[a] Confidence interval was estimated between three parallel experiments with the same material.

Fig. S10 shows the effect of temperature on the rate of NO oxidation to NO_2 for the $Ru_{F,C,Red}$ catalyst. The apparent activation energy (E_a) of 152 kJ/mol is obtained in the temperature range 340–366 °C with a catalytic conversion of 3%–12% at ambient pressure. The activation energy of $Ru_{F,C,Red}$ is much higher than the activation energy of the Pt-based catalysts (ca. 33 kJ/mol) reported by Mulla et al. and Salman et al. [8,15], which may indicate different mechanisms on Pt and Ru catalysts and thereby different rate-determining steps.

The NO oxidation reaction orders with respect to NO, NO_2, O_2 and H_2O at ambient pressure for the $Ru_{F,C,Red}$ catalyst are presented in Fig. S11 and Table 3. An order close to 2 for NO is obtained, along with −1, 1, and 0 for NO_2, O_2, and H_2O respectively. From our reaction order results, it is clear that increasing concentrations of NO_2 in the feed or at high conversion levels, limits oxidation of NO to NO_2 more than H_2O.

3.2.1. Longer isothermal run

Fig. 7a presents a longer isothermal run of conversion of NO to NO_2 along with the outlet oxygen (M/Z = 32) mass spectrometer signal and catalyst bed temperature. The NO to NO_2 conversion increased in the first 8 h and was stable for the rest of the isothermal run. From comparing the extracted region (b) with (c) and (d) in Fig. 7, the NO_2 conversion trend follows the oxygen (M/Z = 32) signal from the mass spectrometer and is also correlated to the catalytic bed temperature.
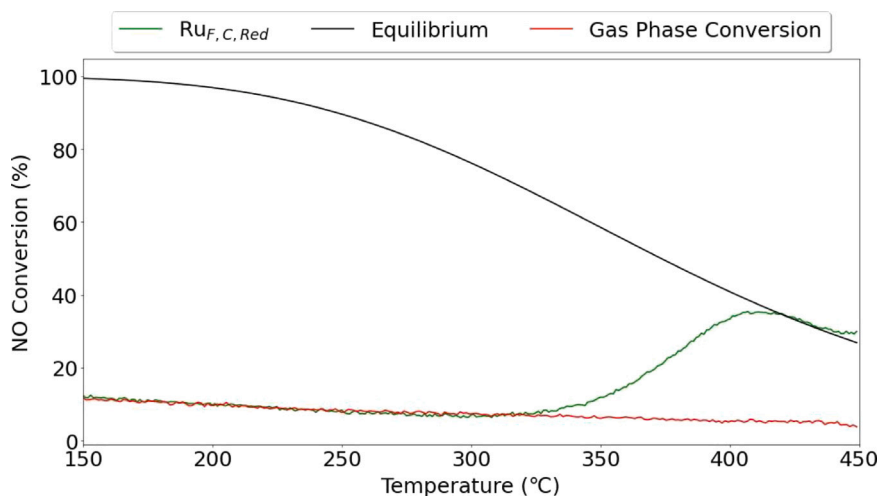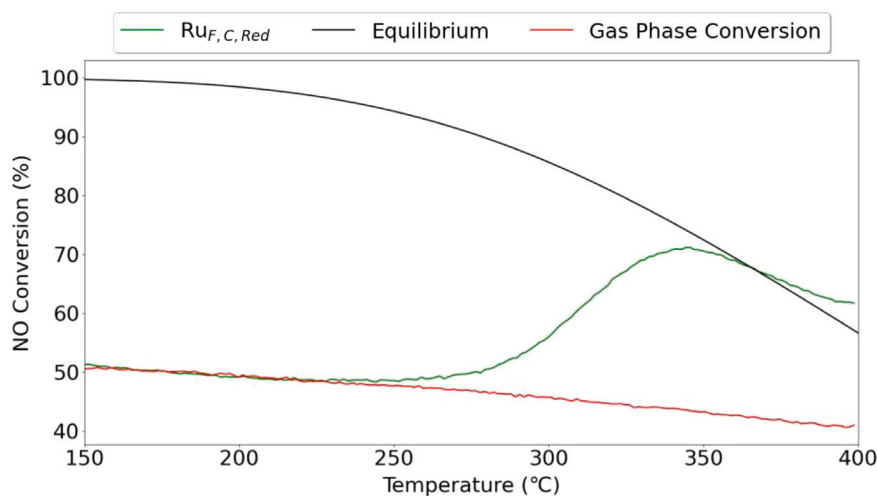
Fig. 5. NO conversion (%) of $Ru_{F,C,Red}$ as a function of temperature with 10% NO, 6% O_2, 15% H_2O and rest Ar, heated at a rate of 5 °C/min at WHSV = 24,000 N cm^3/g$_{gcat}$ h at ambient pressure.

Fig. 6. NO conversion (%) of $Ru_{F,C,Red}$ as a function of temperature with 10% NO, 6% O_2, 15% H_2O and rest Ar, heated at a rate of 5 °C/min at WHSV = 24,000 N cm^3/g$_{gcat}$ h at 4 bar pressure.

The catalytic bed temperature increases as the outlet oxygen MS signal decreases, which indicates oxidation. The spent catalyst X-ray diffractogram after the longer isothermal run ($Ru_{SP,C,Red,LT}$) had no peaks of oxidised ruthenium, but the intensity of metallic ruthenium peaks were lower when compared to the diffractogram of $Ru_{F,C,Red}$ (see Fig. 2).

3.3. In-situ XAS-XRD of NO oxidation

To understand how Ru behaves under NO oxidation conditions, *in-situ* characterisation was performed at BM31 of SNBL, ESRF, France. Figs. 8 and S12 presents *in-situ* XAS-XRD comparison between fresh and spent catalysts together with respective standards. Fig. 9 presents *in-situ* XAS-XRD results of NO oxidation experiment in 0.5%NO, 1.3%O_2. 0.75%H_2O and balance He. The catalysts were pre-reduced in hydrogen by increasing the temperature from 50 to 400 °C, before subjecting it to an isothermal NO oxidation run at 350 °C. All EXAFS spectra and *in-situ* XRD used for analysis (in Figs. 8, S12 and 10) are collected at 50 °C.

From Fig. 8(b) and (c) plots and Fig. S12, the oxidation state of Ru in $Ru_{F,C}$ is +4 (ie RuO_2) and in $Ru_{F,C,Red}$, $Ru_{SP,C,Red}$ Ru appears to be in metallic state. However, close examination of the pseudo radial distribution plots, $Ru_{SP,C,Red}$ appears to be slightly oxidised in comparison to $Ru_{F,C,Red}$ and Ru^0 standard (see (c) in Fig. 8). The intensity of metallic

Ru peaks in $Ru_{SP,C,Red}$ in the *in-situ* X-ray diffractogram is less intense in comparison to the metallic Ru peaks in the $Ru_{F,C,Red}$ diffractogram (see Fig. S12). This was also observed in the *ex-situ* X-ray diffractogram presented in Fig. 2.

Fig. 9 presents *in-situ* XANES data from NO oxidation at 350 °C. MCR analysis was performed on the XANES data and two significant components were extracted (see (b) of Fig. 9). An MCR-calculated contribution plot is presented in (c) of Fig. 9 and an extracted filtered version of the same contribution plot is presented in (e) in Fig. 9 for the time span 50–70 min. The MS signal for O_2 (M/Z = 32) and NO_2 (M/Z = 46) for the extracted time span are presented in Fig. 9(d). A linear combination fitting (LCF) using Athena was also performed on the two MCR-extracted components using RuO_2 and Ru^0 XANES spectra as standards. By comparing the results of *in-situ* XANES (presented in (e) of Fig. 9) and LCF fitting presented in Fig. S16 and Table 4, the ruthenium catalyst goes through cycles of slight oxidation and reduction throughout the NO oxidation isothermal run (see Table 5).

From the *in-situ* XAS-XRD data presented in Figs. 8, S12, 9 and S16, it is clear that during isothermal NO oxidation at 350 °C, Ru goes through a cycle, in which it is slightly oxidised and then reduced for NO_2 generation. Absence of oxidised Ru peaks in the *in-situ* X-ray diffractogram (see $Ru_{SP,C,Red,NO}$ XRD in Fig. 2 and $Ru_{SP,C,Red}$ XRD in Fig. S12) suggests the absence of bulk RuO_2 and the TPR profile of spent
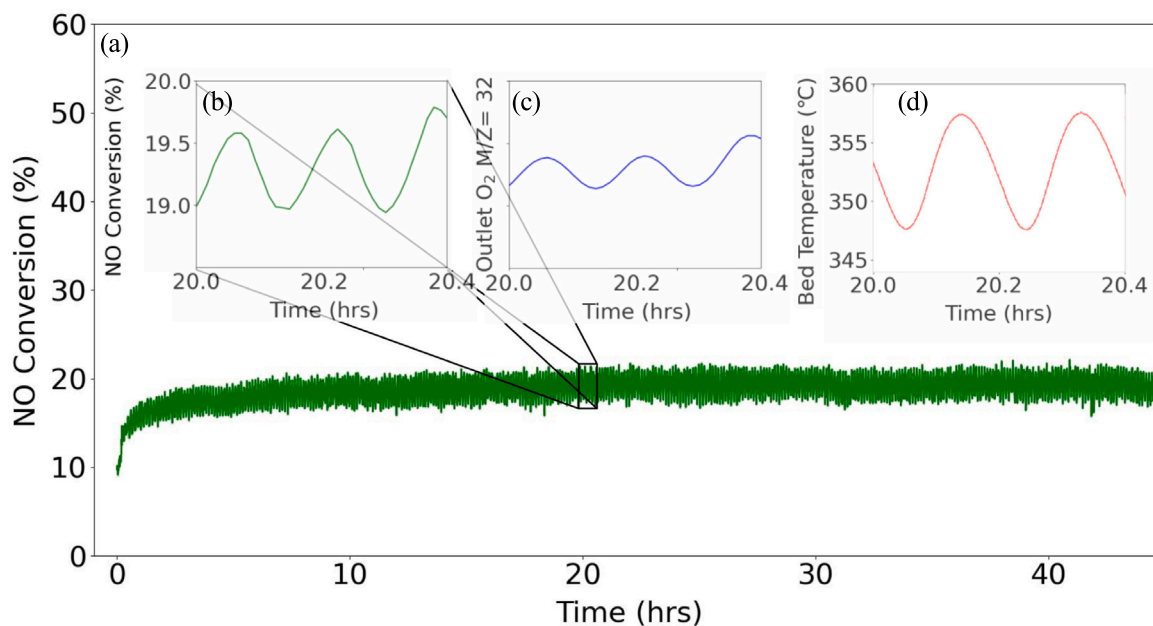
Fig. 7. (a) Longer isothermal experiment showing NO to NO_2 conversion (%) as a function of time at 350 °C with 10% NO, 6% O_2, 15% H_2O and rest Ar, at WHSV = 24,000 N cm^3/g_{gcat} h. (b) Extracted isothermal NO to NO_2 conversion (%) with respect to a time span (20–20.4 h). (c) Extracted outlet mass spectrometer signal of oxygen (M/Z = 32) with respect to a time span (20–20.4 h). (d) Extracted catalytic bed temperature with respect to the same time span (20–20.4 h). Original whole data is presented in Fig. S9.

Table 4

Linear combination fitting (LCF) results for $Ru_{F,C,Red}$ and $Ru_{SP,C,Red}$ from Athena. The reduced χ^2 statistical parameter is used only as a means of relative comparison. Athena uses a nonlinear least-squares minimisation function to fit the data, making it difficult to use the "reduced χ^2" parameter to evaluate the quality of the fits (see Fig. S16).

Sample	Ru^0	Ru^{+4}	Reduced χ^2 (10^{-4})
Component$_A$	99.6%	0.4%	2.6
Component$_B$	71.6%	28.4%	1.1

Table 5

Path, coordination number/number of neighbours (CN), radial distances (R), Debye–Waller factor (σ^2), and R-factor determined by EXAFS fitting of the Ru K edge on $Ru_{F,C,Red}$ and $Ru_{SP,C,Red}$ in k-space, before and after isothermal NO oxidation using Artemis. Fitting of Ru-Ru and Ru-O paths was also performed in k-space using the metallic Ru (Ru^0) and RuO_2 standards respectively.

Catalyst	Path	CN	R (Å)	$\sigma^2 x10^{-3}$ ($Å^2$)	R-factor[a]
Ru^0	Ru-Ru	11.04 ± 0.24	2.67 ± 0.0008	4.45 ± 0.0008	0.15
RuO_2	Ru-O	4.62 ± 0.11	1.99 ± 0.0014	3.0 ± 0.0003	
	Ru-Ru	1.82 ± 0.15	3.10 ± 0.0031	3.8 ± 0.0003	0.15
	Ru-Ru	7.63 ± 0.42	3.55 ± 0.0013	4.9 ± 0.0001	
$Ru_{F,C,Red}$	Ru-Ru	11.57 ± 0.26	2.68 ± 0.0004	5.1 ± 0.0009	0.15
$Ru_{SP,C,Red}$	Ru-Ru	9.42 ± 0.225	2.68 ± 0.0009	5.2 ± 0.0001	0.16
	Ru-O	1.129 ± 0.24	1.91 ± 0.0142	3.3 ± 0.0012	

[a] The reported R-factor is for EXAFS k-space (χ^3) fit with a fitting window of 3–15.1 $Å^{-1}$.

$Ru_{SP,C,Red,NO}$ (see Fig. 3) is consistent with the presence of surface oxidation of Ru, which is in line with our proposed mechanism.

3.4. In-situ DRIFTS during NO oxidation

The $Ru_{F,C,Red}$ catalyst surface was monitored using *in-situ* DRIFTS while NO oxidation was performed. The results from isothermal NO oxidation experiments are presented in Fig. 11 and step experiments are presented in Fig. 12. All collected spectra were converted to absorbance spectra using the background collected at 350 °C in Ar prior to the reaction. IR wavenumbers referred to in Figs. 11 and 12 for different nitrites/nitrates species and Ru-O_x are presented as dashed lines ("– –"). The isothermal NO oxidation experiment was conducted in four steps with IR data collection; (a) the $Ru_{F,C,Red}$ catalyst sample was heated and dwelled at 350 °C in 100% Ar for 30 min, (b) isothermal NO oxidation was performed for 30 min, (c) then isothermal dwell for 30 min in 100% Ar and (d) oxygen purge (in 6%O_2/Ar) for 30 min after the reaction. During initial isothermal dwell in Ar (Fig. 11(a)), no vibrational modes on the catalyst surface were detected. The situation changed as we switched the conditions to NO oxidation. Strong bands appeared in areas corresponding to different kinds of nitrates and nitrites. According to literature, bands around 1230 cm^{-1} attributes to bridging nitrites ((M-O)$_2$ = N) [43], whose presence is not very clear as the IR data gets noisy in that region (presented in Fig. 11(b)). The bands at 1300 cm^{-1} and 1350 cm^{-1} are associated with chelating nitrates (M-2O-N) and nitro compounds (M-NO_2) [22,43], which exhibits intense bands during the NO oxidation reaction (presented in Fig. 11(b)), but are less intense after the reaction (in Ar) and disappears with oxygen purge (presented in Fig. 11(c) and (d)). Much like the bridging nitrite, bands at 1370 cm^{-1} and 1392 cm^{-1} associated with free nitrates (M-NO_3^-) and chelating nitro compounds (M-O-(NO)-M) respectively, are shouldered by nitro compound peaks. A monodentate nitrate (M-O-NO_2) band at 1470 cm^{-1} appeared when oxygen was used to purge the catalyst surface after the reaction (presented in Fig. 11(d)). The bands in the range 1565–1500 cm^{-1} are normally associated with bidentate nitrates (M-O_2NO) and bands at 1650–1580 cm^{-1} are attributed to bridging nitrates ((M-O)$_2$ = NO) [22,43]. Li. et al. [22] associated peaks in the range 1868–1873 cm^{-1} to NO adsorption on RuO_2, and Konstantin [43] associated peaks in the range 1882–1858 cm^{-1} to mononitrosyl adsorption on oxidised ruthenium (Ru^{n+}). Isothermal NO oxidation at 350 °C was also performed on alumina (presented in Fig. S17). There were no notable peaks detected in the range of 2000–1700 cm^{-1}, indicating that the bands found in Fig. 11(b) and (c) in the same range are associated with oxidised ruthenium. Also, less intense bands associated with bridging and bidentate nitrate were found on alumina (see Fig. S17), indicating nitrate formation increased due to the presence of ruthenium. The intense band corresponding to nitro compounds at 1350 cm^{-1} is present during NO oxidation on both the alumina support and the $Ru_{F,C,Red}$ catalyst. From Fig. 11(c), 30 min of evacuation in Ar was not sufficient to remove nitro compounds, but most of the other species desorbed. O_2 purge was required to evacuate nitro compound from the $Ru_{F,C,Red}$ catalyst surface (presented
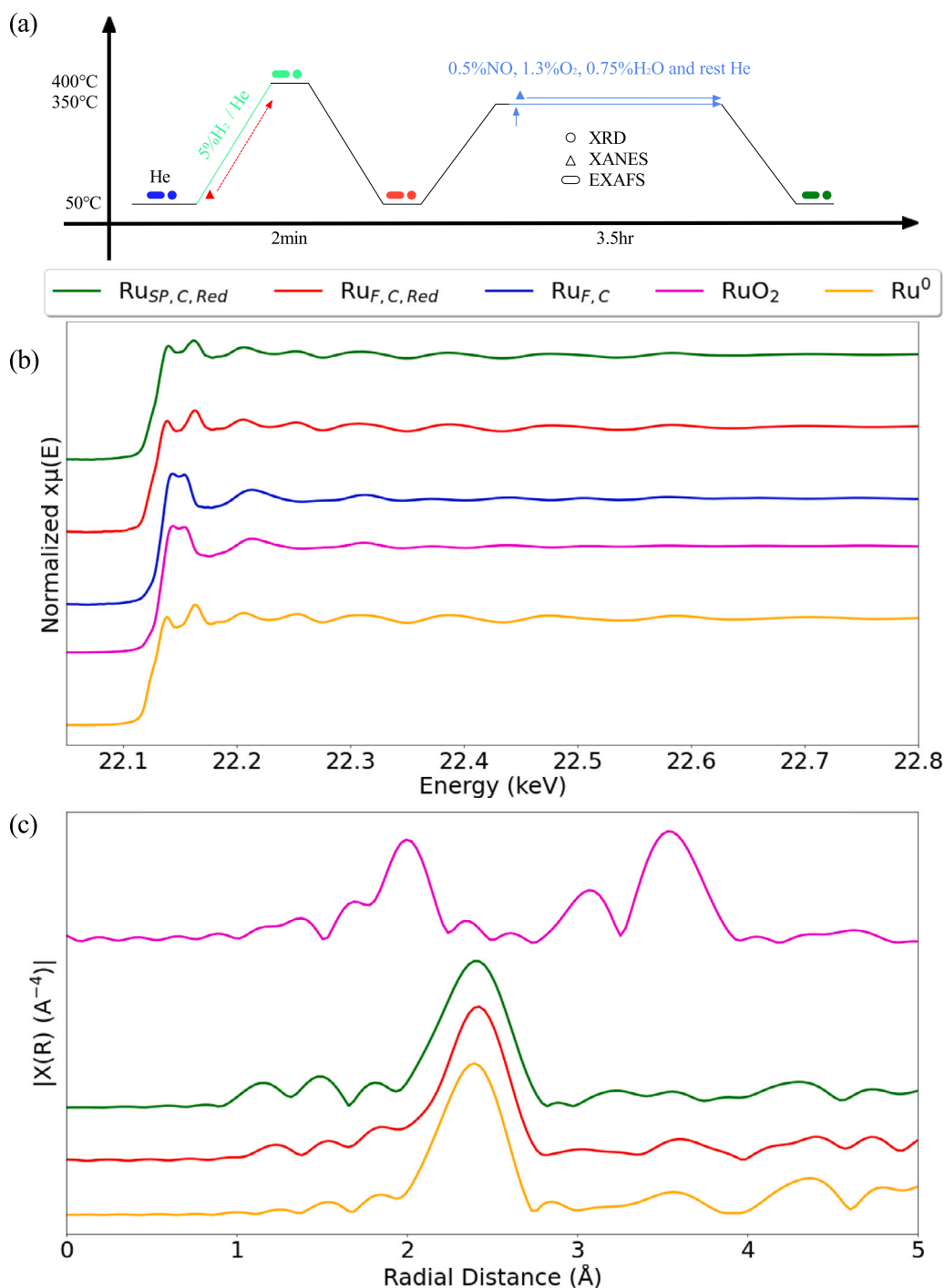
Fig. 8. (a) Overview of the *in-situ* XAS-XRD programme at the Ru K edge. (b) EXAFS profiles collected in He atmosphere at 50 °C at the Ru K edge of $Ru_{F,C}$, $Ru_{F,C,Red}$, $Ru_{SP,C,Red}$, RuO_2 and Ru^0. (c) EXAFS R space plots at Ru K edge of $Ru_{F,C,Red}$, $Ru_{SP,C,Red}$, RuO_2 and Ru^0.

in Fig. 11(d)). During O_2 purge both groups of bands associated with bridging and bidentate nitrates exhibited an increase in intensity followed by a decrease over time. However, the band at 1873 cm^{-1} intensified at the end of the oxygen purge step (presented in Fig. S23). From empty reactor conversion and gas phase NO conversion on alumina presented in Fig. S6, it is clear that alumina alone does not have any NO oxidation activity at 350 °C. Hence, we speculate the presence of these nitrites/nitrates/nitro compounds on alumina as a result of the gas-phase conversion of NO and O_2, while on the $Ru_{F,C,Red}$ catalyst, it is a result of both gas-phase conversion and catalytic activity.

In-situ DRIFTS step experiments were conducted on $Ru_{F,C,Red}$ catalyst at 350 °C (presented in Fig. 12), with each successive six-minute

step and alternating transition between oxygen and nitric oxide in argon. From (a) and (b) of Fig. 12, it can be observed that the band at 1873 cm^{-1} starts increasing in the presence of O_2. As there is no presence of nitric oxide at this stage, the band at 1873 cm^{-1} cannot be associated with nitrosyl adsorption as suggested by Li. et al. [22] and Konstantin [43]. As the conditions are switched to NO/Ar (Fig. 12(c)), the band at 1873 cm^{-1} is sharpened and shifted by 14 cm^{-1}. This band changes shape for every NO-O_2 switch step (step (c) to (d)), and the band was present even when the conditions were switched to 100% Ar (step (g) in Fig. 12). This presence of the band, compared with intense NO_2 signal in the FTIR for every NO-O_2 switch (presented in Fig. S18), indicates desorption of NO_2. There are sharp bands corresponding to
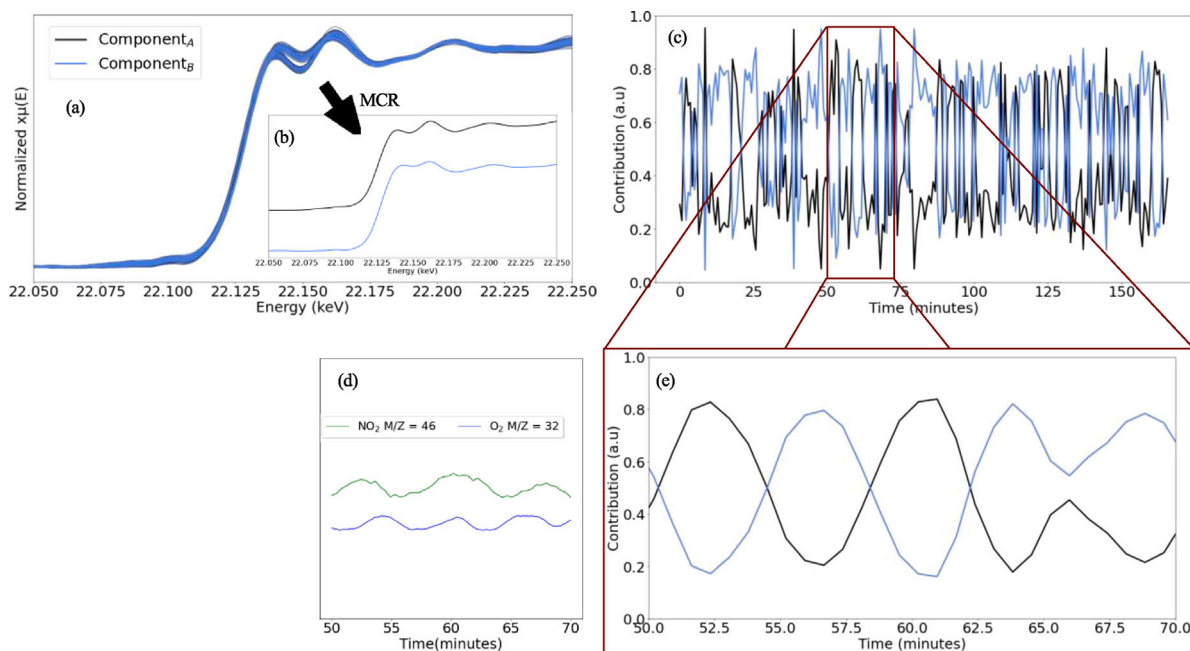
Fig. 9. (a) $Ru_{F,C,Red}$ *in-situ* XANES profiles collected during NO oxidation at 350 °C. (b) MCR extracted components from XANES data in (a). (c) MCR calculated the contribution plot across three hours of XANES data collection. (d) Collected mass spectrometer signal for O_2 and NO_2 during 20 min of total 3 h NO oxidation. (e) Smoothed MCR calculated contribution plot for a time span of 20 min. Fig. S14 presents an error contour plot for MCR analysis and Fig. S15 presents variance for all components obtained using singular value decomposition (SVD).
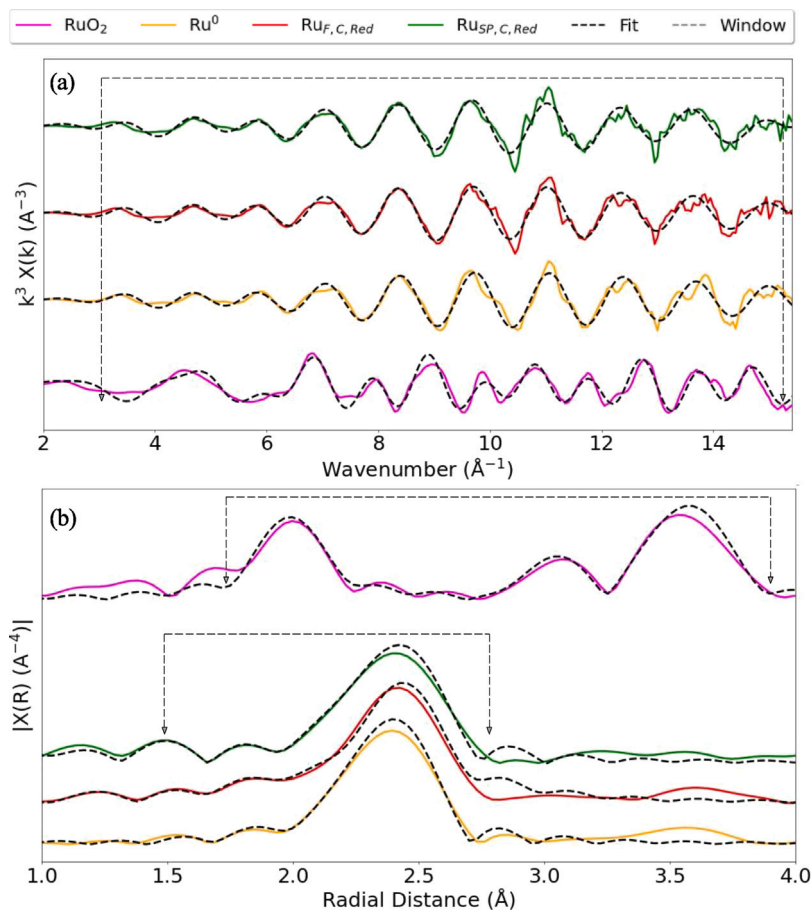

Fig. 10. (a) EXAFS k-space (χ^3) fit as a function of wavenumber for $Ru_{F,C,Red}$, $Ru_{SP,C,Red}$, RuO_2 and Ru^0 with a window of 3–15.1 (b) Visualisation of R space EXAFS fits while fitting in k-space (χ^3) for $Ru_{F,C,Red}$, $Ru_{SP,C,Red}$, and Ru^0 with a window of 1.5–2.75 and RuO_2 fit with a window of 1.75–3.8. Path, coordination number/number of neighbours (CN), radial distances (R), Debye-Waller factor (σ^2), and R-factor for the EXAFS fitting are reported in Table Table 5.
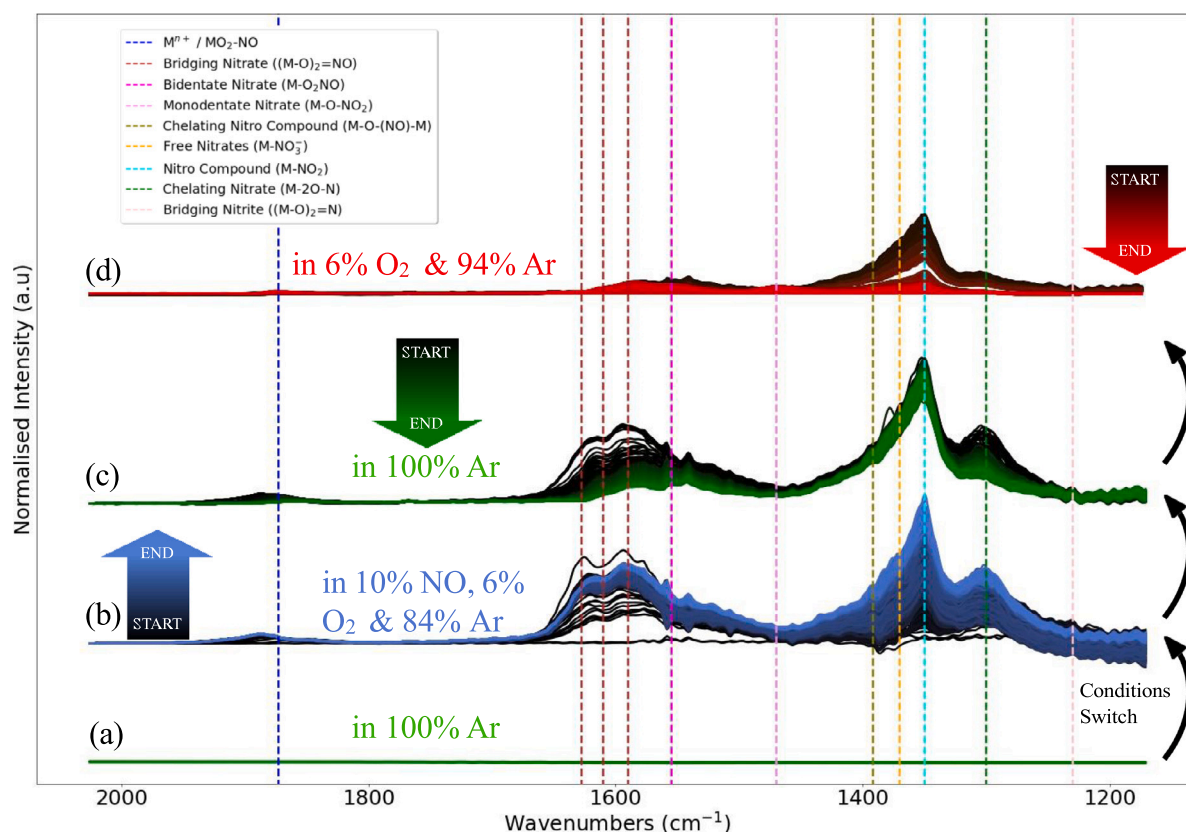
Fig. 11. Normalised stacked 30 min DRIFTS spectra for $Ru_{F,C,Red}$ catalyst at 350 °C in (a) 100% Ar (prior to NO oxidation), (b) 10%NO, 6% O_2 and 84% Ar (NO oxidation), (c) in 100% Ar (post NO oxidation) and (d) 6% O_2/Ar purge (post NO oxidation). Distinct IR bands are marked with respective identified species and are presented as "−−". M in the legend stands for substrate or adsorbent metal.

1650–1580 cm^{-1} bridging and 1565–1500 cm^{-1} bidentate nitrates that were formed initially for every O_2-NO switch step (step (b) to (c)) and slowly became less intense with time, but were present throughout step (c) to (g) of the experiment. This characteristic of an intense band along with intense NO_2 signal in the FTIR (presented in Fig. S18) indicates decomposition of NO_3 to NO_2. A chelating nitro compound band at 1392 cm^{-1} was seen and was present throughout steps (d) to (g) of the experiment with no notable changes.

With every NO-O_2 switch step (step (c) to (d)), the band at 1230 cm^{-1} disappeared with a marginal increase in bridging, bidentate, and chelating nitrate bands and a relatively low NO_2 signal in the FTIR (presented in Fig. S18). This event in connection with the changes in the band at 1873 cm^{-1} suggests that oxygen has the capacity to form surface nitrates. The amount of NO_2 formed is proportional to the intensity of the FTIR signal (presented in Fig. S18), i.e. the more NO_2 the more intense the FTIR gas analyser signal is. The FTIR raw signal is larger during the O_2-NO switch step with diminishing NO_3 DRIFTS IR bands over time than in the NO-O_2 switch step, which indicates the decomposition of nitrates as the most favourable route for NO_2 production. The bands associated with free nitrates, monodentate nitrates, and nitro compounds were absent throughout the step experiments. From Fig. 11(b) and (c), it is observed that the nitro compound band at 1350 cm^{-1} does not disappear after switching to an inert atmosphere. However, other nitrite/nitrate bands slowly become less intense, which indicates strong metal-nitrite interaction. An oxygen purge was required to desorb M-NO_2(strong adsorption) from the catalyst surface ((d) in Fig. 11).

From the results of isothermal NO oxidation and step experiments (presented in Figs. 11, 12 and S18), two discernible regions contributing to the NO_2 product were identified. Region 1 (2000–1730 cm^{-1}) include the band at 1873 cm^{-1} which corresponds to mononitrosyl adsorption on Ru^{n+} [22]. The bands in region 2 (1650–1600 cm^{-1}) are

associated with various types of bridging nitrates. From step experiments ((b)–(c) and (d)–(e) presented in Fig. 12), the band at 1392 cm^{-1} associated with chelating nitro compound also changes in accordance with region 2.

Since the 30 min isothermal NO oxidation DRIFTS data of the $Ru_{F,C,Red}$ catalyst are noisy, MCR analysis was not possible to perform on the entire range of the spectra. Hence, MCR analysis was exclusively carried out only in the range 2000–1730 cm^{-1} (Region 1) and 1650–1600 cm^{-1} (Region 2) for isothermal NO oxidation data of the $Ru_{F,C,Red}$ catalyst (presented in Fig. 11(b)). The MCR results are presented in Fig. S19, S20, S21 and S22, where three components were identified in the analysed spectral range for region 1 and two components for region 2. A clear spectral shift of 14 cm^{-1} was observed during the reaction in region 1. We do not fully understand the spectral shifts in region 1, but we are inclined to think that the spectral shifts between components 2 and 3, and the connected events from step experiments (presented in Fig. 12) are due to mononitrosyl adsorption and desorption on Ru^{n+} during the reaction.

It is unclear how NO oxidation takes place on the intensively studied Pt catalysts at low and high concentrations of NO [15,17,18]. Apart from Li. et al. [22], hardly any literature exists on NO oxidation on Ru or RuO_2 catalysts. Li. et al. [22] applied *in situ* DRIFTS to study Ru/TiO_2 catalysts during NO oxidation at diesel exhaust conditions, where they observed a decrease in adsorption of NO species with increasing temperature and formation of nitrites and bridging nitrates by oxidising NO at 300 °C. They also mentioned that the pathway for NO_2 formation is difficult to distinguish and at temperatures above 275 °C, NO_2 decomposition takes place along with NO oxidation. Stenzel et al. [44] studied NO adsorption on Ru(001) at low temperature (∼−178.15 °C) and ambient temperature, where they observed the formation of an N-O specie at −178.15 °C which disappeared as the temperature increased to room temperature. They also observed that oxidised Ru prevents
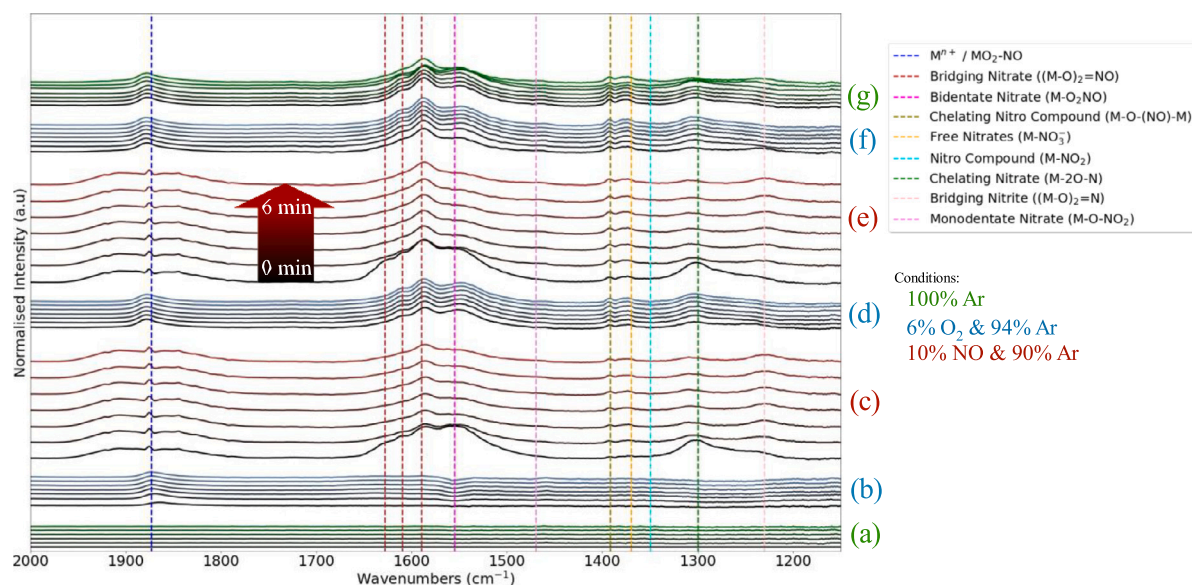
Fig. 12. Stacked DRIFTS spectra for $Ru_{F,C,Red}$ catalyst 6 min step-experiment at 350 °C. (a) $Ru_{F,C,Red}$ catalyst in 100% Ar, (b) $Ru_{F,C,Red}$ catalyst in 6%O_2 and balance Ar, (c) $Ru_{F,C,Red}$ catalyst in 10%NO and balance Ar, (d)$Ru_{F,C,Red}$ catalyst in 6%O_2 and balance Ar, (e) $Ru_{F,C,Red}$ catalyst in 10%NO and balance Ar, (f) $Ru_{F,C,Red}$ catalyst in 6%O_2 and balance Ar and (g) $Ru_{F,C,Red}$ catalyst in 100% Ar. Distinct IR bands are marked with respective identified species and are presented as "– –". M in the legend stands for substrate or adsorbent metal.

the formation of these N-O species on Ru. Martin et al. [45] observed Ru metal oxidation by partial dissociative adsorption of NO, followed by NO chemisorption on oxidised Ru at 299.85 °C. Guglielminotti et al. [46] studied nitric oxide adsorption on reduced and oxidised Ru catalysts and found that NO is likely to adsorb more on oxidised Ru at temperatures higher than 250 °C. Sokolova et al. [47] examined nitric oxide adsorption and decomposition chemistry on ruthenium black and alumina-supported ruthenium catalysts. The work concluded that NO adsorption proceeds via nitrite and nitrate complex routes and also that NO is more likely to adsorb on oxidised Ru at temperatures above 300 °C.

From oxygen adsorption studies on single-atomic ruthenium, oxygen was found to adsorb dissociatively on Ru at ambient temperatures [48]. According to Montemore et al. [49], O_2 tends to dissociatively adsorb on Ru(0001) even at 100 K for low oxygen coverages, while at high coverages, O_2 tends to chemisorb. DFT studies indicated a stable peroxo O_2 state on Ru surfaces with a low dissociation barrier [49]. Diulus et al. [50] studied thermal oxidation of Ru to RuO_2 using XPS, where they observed the formation of meta-stable O-Ru-O structures at 350 °C.

Salman et al. [8] proposed a Langmuir-Hinshelwood mechanism with NO as the most abundant reaction intermediate and desorption of NO_2 as the rate-limiting step for Pt/γ-Al_2O_3 catalyst. The above-mentioned literature studies clearly stipulate that oxygen tends to chemisorb or dissociatively adsorb on metallic Ru, whereas adsorption of NO is preferred on oxidised Ru forming nitrite/nitrates on the RuO_x surface.

From *in-situ* XANES and EXAFS we hypothesise that surface oxidation of ruthenium takes place during NO oxidation (see Figs. 8–10). The absence of RuO_2 peaks in the *in-situ* and *ex-situ* X-ray diffractograms of the spent catalyst samples (presented in Figs. 2 and S12) indicates that bulk ruthenium oxides are not formed. The H_2-TPR profile of the $Ru_{SP,C,Red,NO}$ catalyst exhibited an easily removable oxide, most likely related to the catalyst surface. It was clearly observed that the catalyst surface was oxidised at the end of both DRIFTS experiments (presented in Figs. 11, 12 and S23). XPS results (presented in Fig. 4) verify this hypothesis.

45 h long isothermal activity measurements (presented in Fig. 7) and MCR analysis on *in-situ* XANES (Fig. 9) and DRIFTS NO oxidation (Figs. 11, S19 and S21) data provided insights regarding catalyst

stability and the cyclic process of oxidation and reduction for NO_2 generation.

From the above results and literature, we propose that the first step to NO oxidation is the dissociative adsorption of oxygen on the ruthenium surface, followed by nitrites and nitrates formation due to the interaction with NO. The latter hypothesis leads to a non-elementary reaction step and is purely based on DRIFTS results (presented in Figs. 11 and 12). The strong adsorption of NO_2 (presented in Figs. 11 and S23)and its disappearance due to the O_2 purge indicates this to be a limiting step for NO oxidation on the ruthenium-alumina catalyst. Comparing the raw FTIR signals during the O_2-NO switch step with the NO-O_2 switch step, indicates the decomposition of nitrates as the most favourable route for NO_2 production (presented in Figs. 12 and S18). Hence, we propose the following Eley-Rideal mechanism for NO oxidation with NO adsorbing on oxidised Ru, with nitrites/nitrates formation and further generation of gaseous NO_2 by dissociation of adsorbed NO_3:

$$O_2 + 2* \xrightleftharpoons{K_1} 2O^* \qquad (6)$$

$$2NO + 3O^* \xrightleftharpoons{K_2} NO_3^* + NO_2^* + * \qquad (7)$$

$$NO_3^* \xrightleftharpoons{K_3} NO_2 + O^* \qquad (8)$$

$$NO_2^* + 0.5O_2 \xrightarrow{k_4} NO_3^* \qquad (9)$$

Here * represents a free active site, k_i and K_i denotes rate constants and equilibrium constants respectively. Since oxygen adsorption is a necessity for NO adsorption, we assume O as the MARI and NO_3 generation by NO_2^*-O_2 interaction as the rate-limiting step. The rate can be expressed as:

$$r = \frac{K_1.K_2.k_4.P_{NO}^2.P_{O_2}.(P_{O_2})^{0.5}}{K_3.P_{NO_2}.(1+(K_1.P_{O_2})^{0.5})} \qquad (10)$$

When the surface coverage of adsorbed O is larger than the fraction of free sites, $\theta_O \gg 1$. The rate expression simplifies to:

$$r = \frac{(K_1)^{0.5}.K_2.k_4.P_{NO}^2.P_{O_2}}{K_3.P_{NO_2}} \qquad (11)$$

$$r = \frac{k_4 . K_G . P_{NO}^2 . P_{O_2}}{P_{NO_2}} \tag{12}$$

where $K_G = ((K_1)^{0.5} . K_2 / K_3)$. No other mechanism was found to satisfy experimental observations and the state of ruthenium in the presence of oxygen.

4. Conclusions

NO oxidation activity of 0.5 wt.% Ru/γ-Al$_2$O$_3$ catalyst was studied with a feed containing 10% NO, 6% O$_2$, 15% H$_2$O and balance Ar at ambient and 4 bar pressures, simulating close to industrial nitric acid conditions. The effect of pressure and temperature was investigated at nitric acid synthesis conditions, and a suitable reaction mechanism was proposed.

The reduced Ru catalyst exhibited high catalytic activity, showing a maximum conversion level of 72% at 4 bar pressure in 10% NO, 6% O$_2$, 15% H$_2$O and balance Ar. Increasing the pressure to 4 bar shifted the maximum catalytic activity to a lower temperature (340 °C) than obtained at ambient pressure (420 °C). At ambient pressure, an apparent activation energy of 152 kJ/mol was found. The NO oxidation reaction was found to be second order with respect to NO, first order with respect to O$_2$ and inversely dependent on the NO$_2$ partial pressure. The inverse dependency on the product NO$_2$, indicates that the reaction is favourable at higher temperatures (lower gas-phase oxidation), which is in line with previous studies on NO oxidation at various NO concentrations. The catalyst was also stable throughout 45 h of isothermal NO oxidation at ambient pressure. *In-situ* XAS-XRD and DRIFTS experiments revealed the redox mechanism on how the catalyst generates NO$_2$. These results illustrate that the alumina-supported ruthenium catalysts are promising catalysts for industrial nitric acid production.

CRediT authorship contribution statement

Jithin Gopakumar: Conceptualization, Methodology, Validation, Formal analysis, Investigation, Writing – original draft, Writing – review & editing, Visualization. **Pål Martin Benum:** Investigation, Formal analysis, Validation. **Ingeborg-Helene Svenum:** Investigation, Formal analysis, Validation. **Bjørn Christian Enger:** Conceptualization, Validation, Writing – review & editing, Supervision, Funding acquisition . **David Waller:** Conceptualization, Validation, Writing – review & editing, Supervision, Funding acquisition . **Magnus Rønning:** Conceptualization, Validation, Writing – review & editing, Supervision, Project administration, Funding acquisition.

Declaration of competing interest

The authors declare that they have no known competing financial interests or personal relationships that could have appeared to influence the work reported in this paper.

Data availability

Data will be made available on request.

Acknowledgements

Appendix A. Supplementary data

Supplementary material related to this article can be found online at https://doi.org/10.1016/j.cej.2023.146406.

References

[1] Michael Thiemann, Erich Scheibler, Karl Wilhelm Wiegand, Nitric acid, nitrous acid, and nitrogen oxides, in: Ullmann's Encyclopedia of Industrial Chemistry, Wiley-VCH Verlag GmbH & Co. KGaA, Weinheim, Germany, 2000.

[2] Murray Park, International Fertilizer Industry Association, The Fertilizer Industry, Elsevier, 2001, p. iv.

[3] György D. Honti, The Nitrogen Industry, Vol. 48, 1976 ed., Akadémiai Kiadó, 1976.

[4] Anthony S. Travis, Nitrogen Capture, Springer International Publishing, Cham, 2018.

[5] Jacob A. Moulijn, Chemical process technology, Choice Rev. Online 51 (04) (2013) 51–2107.

[6] Willis A. Rosser, Henry Wise, Thermal decomposition of nitrogen dioxide, J. Chem. Phys. 24 (2) (1956) 493–494.

[7] Carlos A. Grande, Kari Anne Andreassen, Jasmina H. Cavka, David Waller, Odd Arne Lorentsen, Halvor Øien, Hans Jörg Zander, Stephen Poulston, Sonia García, Deena Modeshia, Process intensification in nitric acid plants by catalytic oxidation of nitric oxide, Ind. Eng. Chem. Res. 57 (31) (2018) 10180–10186.

[8] Ata ul Rauf Salman, Bjørn Christian Enger, Xavier Auvray, Rune Lødeng, Mohan Menon, David Waller, Magnus Rønning, Catalytic oxidation of NO to NO2 for nitric acid production over a Pt/Al2O3 catalyst, Appl. Catal. A: Gen. 564 (2) (2018) 142–146.

[9] Ata Ul Rauf Salman, Signe Marit Hyrve, Samuel Konrad Regli, Muhammad Zubair, Bjørn Christian Enger, Rune Lødeng, David Waller, Magnus Rønning, Catalytic oxidation of NO over LaCo1-xBxO3 (B = Mn, Ni) perovskites for nitric acid production, Catalysts 9 (5) (2019) 429.

[10] Jithin Gopakumar, Sunniva Vold, Bjørn Christian Enger, David Waller, Per Erik Vullum, Magnus Rønning, Catalytic oxidation of NO to NO 2 for industrial nitric acid production using Ag-promoted MnO 2 /ZrO 2 catalysts, Catal. Sci. Technol. 13 (9) (2023) 2783–2793.

[11] William C. Klingelhoefer, Syracuse, Nitric oxide oxidation, 1938.

[12] Morton L. Heilig, Process of oxidizing gases, ACM SIGGRAPH Comput. Graph. 28 (2) (1994) 131–134.

[13] Hogler C. Andersen, Alfred J. Haley, Process for the oxidation of nitric oxide, 1963.

[14] Zhe Hong, Zhong Wang, Xuebing Li, Catalytic oxidation of nitric oxide (NO) over different catalysts: an overview, Catal. Sci. Technol. 7 (16) (2017) 3440–3452.

[15] S.S. Mulla, N. Chen, W.N. Delgass, W.S. Epling, F.H. Ribeiro, NO 2 inhibits the catalytic reaction of NO and O 2 over Pt, Catal. Lett. 100 (3–4) (2005) 267–270.

[16] Brian M. Weiss, Enrique Iglesia, E.O. Lawrence Berkeley, NO oxidation catalysis on Pt clusters : Elementary steps , structural requirements , and synergistic effects of NO 2 adsorption sites, (2) (2009) 13331–13340.

[17] Louise Olsson, Hans Persson, Erik Fridell, Magnus Skoglundh, Bengt Andersson, A kinetic study of NO oxidation and NOx storage on Pt/Al2O3 and Pt/BaO/Al2O3, J. Phys. Chem. B 105 (29) (2001) 6895–6906.

[18] Louise Olsson, Erik Fridell, The influence of Pt oxide formation and Pt dispersion on the reactions, J. Catalysis 353 (2) (2002) 340–353.

[19] Chaitanya K. Narula, Lawrence F. Allard, G.M. Stocks, Melanie Moses-DeBusk, Remarkable NO oxidation on single supported platinum atoms, Sci. Rep. 4 (1) (2015) 7238.

[20] Kazijo Urabe, Takashi Yoshioka, Atsumu Ozaki, Ammonia Synthesis Activity of a Raney Ruthenium Catalyst, Technical report, 1978, pp. 52–56.

[21] Huazhang Liu, Ammonia synthesis catalyst 100 years: Practice, enlightenment and challenge, Chin. J. Catal. 35 (10) (2014) 1619–1640.

[22] Landong Li, Lingling Qu, Jie Cheng, Jinjun Li, Zhengping Hao, Oxidation of nitric oxide to nitrogen dioxide over Ru catalysts, Appl. Catal. B 88 (1–2) (2009) 224–231.

[23] Herbert Over, Surface chemistry of ruthenium dioxide in heterogeneous catalysis and electrocatalysis: From fundamental to applied research, Chem. Rev. 112 (6) (2012) 3356–3426.

[24] Han Bom Kim, Eun Duck Park, Ammonia decomposition over Ru catalysts supported on alumina with different crystalline phases, Catal. Today 411–412 (2023) 113817.

[25] Yaru Zhang, Xiaoli Yang, Xiaofeng Yang, Hongmin Duan, Haifeng Qi, Yang Su, Binglian Liang, Huabing Tao, Bin Liu, De Chen, Xiong Su, Yanqiang Huang, Tao Zhang, Tuning reactivity of Fischer–Tropsch synthesis by regulating TiOx overlayer over Ru/TiO2 nanocatalysts, Nature Commun. 11 (1) (2020) 3185.

[26] Neal Fairley, Vincent Fernandez, Mireille Richard-Plouet, Catherine Guillot-Deudon, John Walton, Emily Smith, Delphine Flahaut, Mark Greiner, Mark Biesinger, Sven Tougaard, David Morgan, Jonas Baltrusaitis, Systematic and collaborative approach to problem solving using X-ray photoelectron spectroscopy, Appl. Surf. Sci. Adv. 5 (2021) 100112.

[27] David J. Morgan, Resolving ruthenium: XPS studies of common ruthenium materials, Surf. Interface Anal. 47 (11) (2015) 1072–1079.

[28] Chen Zheng, Kiran Mathew, Chi Chen, Yiming Chen, Hanmei Tang, Alan Dozier, Joshua J. Kas, Fernando D. Vila, John J. Rehr, Louis F.J. Piper, Kristin A. Persson, Shyue Ping Ong, Automated generation and ensemble-learned matching of X-ray absorption spectra, npj Comput. Mater. 4 (1) (2018) 12.

[29] Kiran Mathew, Chen Zheng, Donald Winston, Chi Chen, Alan Dozier, John J. Rehr, Shyue Ping Ong, Kristin A. Persson, High-throughput computational X-ray absorption spectroscopy, Sci. Data 5 (1) (2018) 180151.

[30] Anubhav Jain, Shyue Ping Ong, Geoffroy Hautier, Wei Chen, William Davidson Richards, Stephen Dacek, Shreyas Cholia, Dan Gunter, David Skinner, Gerbrand Ceder, Kristin A. Persson, Commentary: The Materials Project: A materials genome approach to accelerating materials innovation, APL Mater. 1 (1) (2013).

[31] Yiming Chen, Chi Chen, Chen Zheng, Shyam Dwaraknath, Matthew K. Horton, Jordi Cabana, John Rehr, John Vinson, Alan Dozier, Joshua J. Kas, Kristin A. Persson, Shyue Ping Ong, Database of ab initio L-edge X-ray absorption near edge structure, Sci. Data 8 (1) (2021) 153.

[32] Charles H. Camp, PyMCR: A python library for multivariate curve resolution analysis with alternating regression (MCR-AR), J. Res. Natl. Inst. Stand. Technol. 124 (2019) 124018.

[33] Pauli Virtanen, Ralf Gommers, Travis E. Oliphant, Matt Haberland, Tyler Reddy, David Cournapeau, Evgeni Burovski, Pearu Peterson, Warren Weckesser, Jonathan Bright, Stéfan J. van der Walt, Matthew Brett, Joshua Wilson, K. Jarrod Millman, Nikolay Mayorov, Andrew R.J. Nelson, Eric Jones, Robert Kern, Eric Larson, C.J. Carey, İlhan Polat, Yu Feng, Eric W. Moore, Jake VanderPlas, Denis Laxalde, Josef Perktold, Robert Cimrman, Ian Henriksen, E.A. Quintero, Charles R. Harris, Anne M. Archibald, Antônio H. Ribeiro, Fabian Pedregosa, Paul van Mulbregt, Aditya Vijaykumar, Alessandro Pietro Bardelli, Alex Rothberg, Andreas Hilboll, Andreas Kloeckner, Anthony Scopatz, Antony Lee, Ariel Rokem, C. Nathan Woods, Chad Fulton, Charles Masson, Christian Häggström, Clark Fitzgerald, David A. Nicholson, David R. Hagen, Dmitrii V. Pasechnik, Emanuele Olivetti, Eric Martin, Eric Wieser, Fabrice Silva, Felix Lenders, Florian Wilhelm, G. Young, Gavin A. Price, Gert-Ludwig Ingold, Gregory E. Allen, Gregory R. Lee, Hervé Audren, Irvin Probst, Jörg P. Dietrich, Jacob Silterra, James T Webber, Janko Slavič, Joel Nothman, Johannes Buchner, Johannes Kulick, Johannes L. Schönberger, José Vinícius de Miranda Cardoso, Joscha Reimer, Joseph Harrington, Juan Luis Cano Rodríguez, Juan Nunez-Iglesias, Justin Kuczynski, Kevin Tritz, Martin Thoma, Matthew Newville, Matthias Kümmerer, Maximilian Bolingbroke, Michael Tartre, Mikhail Pak, Nathaniel J. Smith, Nikolai Nowaczyk, Nikolay Shebanov, Oleksandr Pavlyk, Per A. Brodtkorb, Perry Lee, Robert T. McGibbon, Roman Feldbauer, Sam Lewis, Sam Tygier, Scott Sievert, Sebastiano Vigna, Stefan Peterson, Surhud More, Tadeusz Pudlik, Takuya Oshima, Thomas J. Pingel, Thomas P. Robitaille, Thomas Spura, Thouis R. Jones, Tim Cera, Tim Leslie, Tiziano Zito, Tom Krauss, Utkarsh Upadhyay, Yaroslav O. Halchenko, Yoshiki Vázquez-Baeza, SciPy 1.0: fundamental algorithms for scientific computing in Python, Nature Methods 17 (3) (2020) 261–272.

[34] B. Ravel, M. Newville, ATHENA , ARTEMIS , HEPHAESTUS : data analysis for X-ray absorption spectroscopy using IFEFFIT, J. Synchrotron Radiat. 12 (4) (2005) 537–541.

[35] H. Scott Fogler, Elements of Chemical Reaction Engineering, 2006.

[36] Vijay Narkhede, Jens Aßmann, Martin Muhler, Structure-Activity Correlations for the Oxidation of CO over Polycrystalline RuO 2 Powder Derived from Steady-State and Transient Kinetic Experiments, Technical report, 2005, pp. 979–995.

[37] Ioan Balint, Akane Miyazaki, Ken-ichi Aika, Chemical and morphological evolution of supported Ru nanoparticles during oxidative conversion of methane, React. Kinetics Catal. Lett. 80 (1) (2003) 81–87.

[38] P. Betancourt, A. Rives, R. Hubaut, C.E. Scott, J. Goldwasser, A Study of the Ruthenium±alumina System, Technical report.

[39] Jian Shi, Feng Hui, Jun Yuan, Qinwei Yu, Suning Mei, Qian Zhang, Jialin Li, Weiqiang Wang, Jianming Yang, Jian Lu, Ru-Ti oxide based catalysts for HCl oxidation: The favorable oxygen species and influence of Ce additive, Catalysts 9 (2) (2019) 108.

[40] Xiaobo Fu, Hao Yu, Feng Peng, Hongjuan Wang, Yu Qian, Facile preparation of RuO2/CNT catalyst by a homogenous oxidation precipitation method and its catalytic performance, Appl. Catal. A: Gen. 321 (2) (2007) 190–197.

[41] A. Roine, HSC chemistry® [Software],Metso Outotec, Pori, 2021.

[42] Oleksii Bezkrovnyi, Mykhailo Vorokhta, Mirosława Pawlyta, Maciej Ptak, Lesia Piliai, Xianxian Xie, Thu Ngan Dinhová, Ivan Khalakhan, Iva Matolínová, Leszek Kepinski, In situ observation of highly oxidized Ru species in Ru/CeO2 catalyst under propane oxidation, J. Mater. Chem. A 10 (31) (2022) 16675–16684.

[43] Konstantin I. Hadjiivanov, Identification of neutral and charged N x O y surface species by IR spectroscopy, Catal. Rev. 42 (1–2) (2000) 71–144.

[44] W. Stenzel, H. Conrad, B.E. Hayden, K. Kretschmar, A.M. Bradshaw, The adsorption of NO on Ru(001) and its CO-adsorption with oxygen studied by vibrational spectroscopy, in: Studies in Surface Science and Catalysis, Vol. 14, 1983, p. 261.

[45] R.L. Martins, M.A.S. Baldanza, M. Schmal, An infrared study of NO and CO adsorption on zeolite-supported Ru and Ru–Pt catalysts, J. Phys. Chem. B 105 (42) (2001) 10303–10307.

[46] E. Guglielminotti, F. Boccuzzi, Nitric oxide adsorption and nitric oxide-carbon monoxide interaction on Ru/ZnO catalyst, J. Catalysis 141 (2) (1993) 486–493.

[47] L.A. Sokolova, N.M. Popova, K. Dosumov, Mechanism of NO adsorption and decomposition on ruthenium catalysts, React. Kinetics Catal. Lett. 26 (1–2) (1984) 193–197.

[48] Linlin Cao, Qiquan Luo, Jiajia Chen, Lan Wang, Yue Lin, Huijuan Wang, Xiaokang Liu, Xinyi Shen, Wei Zhang, Wei Liu, Zeming Qi, Zheng Jiang, Jinlong Yang, Tao Yao, Dynamic oxygen adsorption on single-atomic Ruthenium catalyst with high performance for acidic oxygen evolution reaction, Nature Commun. 10 (1) (2019).

[49] Matthew M. Montemore, Matthijs A. Van Spronsen, Robert J. Madix, Cynthia M. Friend, O2 activation by metal surfaces: Implications for bonding and reactivity on heterogeneous catalysts, Chem. Rev. 118 (5) (2018) 2816–2862.

[50] J. Trey Diulus, Benjamin Tobler, Jürg Osterwalder, Zbynek Novotny, Thermal oxidation of Ru(0001) to RuO2(110) studied with ambient pressure x-ray photoelectron spectroscopy, J. Phys. D: Appl. Phys. 54 (24) (2021).